THE DISCOVERY OF EXTENDED THERMAL X-RAY EMISSION FROM PKS 2152−699: EVIDENCE FOR A "JET-CLOUD" INTERACTION

CHUN LY,[1] DAVID S. DE YOUNG,[2] AND JILL BECHTOLD[3]

ABSTRACT

A *Chandra* ACIS-S observation of PKS 2152−699 reveals thermal emission from a diffuse region around the core and a hotspot located $10''$ northeast from the core. This is the first detection of thermal X-ray radiation on kiloparsec scales from an extragalactic radio source. Two other hotspots located $47''$ north-northeast and $26''$ southwest from the core were also detected. Using a Raymond-Smith model, the first hotspot can be characterized with a thermal plasma temperature of 2.6×10^6 K and an electron number density of 0.17 cm^{-3}. These values correspond to a cooling time of $\sim 1.6 \times 10^7$ yr. In addition, an emission line from the hotspot, possibly Fe xxv, was detected at rest wavelength 10.04 Å. The thermal X-ray emission from the first hotspot is offset from the radio emission but is coincident with optical filaments detected with broadband filters of *Hubble Space Telescope* WFPC2. The best explanation for the X-ray, radio, and optical emission is that of a "jet-cloud" interaction. The diffuse emission around the nucleus of PKS 2152−699 can be modeled as a thermal plasma with a temperature of 1.2×10^7 K and a luminosity of 1.8×10^{41} ergs s^{-1}. This emission appears to be asymmetric, with a small extension toward hotspot A, similar to a jet. An optical hotspot (extended emission-line region) is seen less than $1''$ away from this extension in the direction of the core. This indicates that the extension may be caused by the jet interacting with an inner interstellar medium cloud, or that it is due to entrainment of hot gas. Future observations are discussed.

Subject headings: galaxies: active — galaxies: individual (PKS 2152−699) — galaxies: jets — galaxies: kinematics and dynamics

1. INTRODUCTION

Radio images have shown that jets of radio galaxies disperse on kiloparsec or megaparsec scales, forming hotspots and lobes at the end of the jet's path. The formation of these lobes is believed to be caused by the interaction between a jet propagating through the interstellar or the intergalactic medium (e.g., De Young 2002). In principle, the jet may be deflected by a dense inhomogeneity in the ambient medium, and past three-dimensional numerical simulations have examined the physics of this interaction (De Young 1991; Higgins et al. 1999; Wang et al. 2000).

When a jet interacts with the ambient medium, shocks are likely to form, producing extended emission lines in the UV, optical, and X-rays through ionization of the medium (Tadhunter 2002). Powerful radio galaxies that may have undergone jet-cloud interactions that cause their extended emission-line regions (EELRs) are 3C 277.3 (van Breugel et al. 1985; Tadhunter et al. 2000; Solórzano-Iñarrea & Tadhunter 2003), 3C 265 (Solórzano-Iñarrea & Tadhunter 2003), PKS 2250−41 (Villar-Martín et al. 1999), and PKS 2152−699 (Tingay et al. 1996; Fosbury et al. 1998).

PKS 2152−699, a well-studied Fanaroff-Riley type II radio galaxy (Fanaroff & Riley 1974) at $z = 0.0283$, is one of the brightest sources in the southern sky, with a flux of ~ 19 Jy at 2.7 GHz (Wall 1994). In addition, this source is quite isolated: the nearest galaxy is 250 kpc away and less than 50 galaxies are within a 3 Mpc radius (Tadhunter et al. 1988). Previously,

Tadhunter et al. (1988), Tingay et al. (1996), and Fosbury et al. (1998) have suggested that the deflection of the northern jet is conceivably caused by a "jet-cloud" interaction. For example, radio observations obtained from the Australia Telescope Compact Array (ATCA) reveal a hotspot (hereafter hotspot A) located $\sim 10''$ northeast from the core. The detection of the northern lobe and hotspot (hereafter hotspot B) indicates a $20°$ deflection in the jet (Tingay et al. 1996; Fosbury et al. 1998). In this paper, the analysis of archival data from the *Chandra X-Ray Observatory* is presented as evidence for a jet-cloud interaction occurring at hotspot A and the extension near the core in PKS 2152−699.

In § 2, the X-ray observation is presented and compared with previously obtained radio and optical images. The analysis of X-ray spectra and the core's point-spread function (PSF) are provided in § 3. In § 4, a jet-cloud interaction is presented to explain hotspot A and the northeastern, extended thermal emission. Section 5 describes possible future observations, and concluding remarks are made in the final section.

2. OBSERVATIONS

2.1. *Radio and Optical Observations*

The ATCA was used by Fosbury et al. (1998) to observe PKS 2152−699 at 3.5 cm (8.64 GHz) on 1992 January 19 and at 6.3 cm (4.74 GHz) on 1992 April 1. In addition, a *Hubble Space Telescope* (*HST*) WFPC2 observation (Proposal 5479; PI: M. Malkan) published in Fosbury et al. (1998) was obtained with the F606W filter on 1994 October 20. The reduced radio and optical images were provided by Fosbury et al.

2.2. *X-Ray Observation*

PKS 2152−699 was observed (observation ID 1627; PI: A. Wilson) with the *Chandra* Advanced CCD Imaging

[1] Current address: Department of Astronomy, University of California at Los Angeles, Box 951547, Los Angeles, CA 90095-1547; chun@astro.ucla.edu.
[2] National Optical Astronomy Observatory, 950 North Cherry Avenue, Tucson, AZ 85719; ddeyoung@noao.edu.
[3] Steward Observatory, University of Arizona, 933 North Cherry Avenue, Tucson, AZ 85721; jbechtold@as.arizona.edu.

Spectrometer (ACIS-S)[4] without a transmission grating in place on 2001 August 2 for approximately 14 ks. The level 1 products were obtained directly from the archive, where they went through standard data processing with the afterglow correction removed (see § 3.3). In this observation, the core with diffuse emission around it and three hotspots were detected, as shown by the contours in Figure 1. The most prominent hotspot is located $10''$ (5.6 kpc, P.A. $137°$) from the core. Here $1''$ corresponds to 0.56 kpc under the assumption that $H_0 = 71$ km s^{-1} Mpc^{-1}, $\Omega_\lambda = 0.73$, and $\Omega_m = 0.27$ (Bennett et al. 2003). The other two hotspots, B and C, were detected $47''$ (26.3 kpc, P.A. $116°$) and $26''$ (14.6 kpc, P.A. $292°$) from the core.

The X-ray contours in Figure 1 reveal that the diffuse emission is extended more toward the northeast. This extension (labeled as E) is similar to a jet when it is compared with the 3.5 cm radio jet as shown in Figure 2. The purple line shows that the radio jet propagates toward hotspot A's X-ray emission. In addition, the diffuse emission extends in the east-west direction, as noted by the low-level contours in Figure 1.

2.3. Positional Corrections in Images

Prior to overlaying these images, positional corrections relative to the International Celestial Reference Frame Extension 1 (ICRF-Ext. 1) coordinates were made (Ma et al. 1998; IERS 1999). The offsets (σ_α, σ_δ) between the ICRF-Ext. 1 coordinates and the *Chandra* and *HST* coordinates are ($0''.1$, $-0''.1$) and ($-1''.4$, $-0''.1$), respectively. The radio observations had a correction of ($-0''.4$, $-0''.3$). The X-ray position agrees with surveys[5] indicating an offset within $0''.4$ relative to the ICRF-Ext. 1, and the optical offsets are reasonable compared with the point inaccuracy of $0''.26$–$1''.84$ (Biretta et al. 1996). These images were imported into the Astronomical Image Processing System (AIPS), where the package HGEOM was used to geometrically align the images together.

2.4. Multiwavelength Overlays

In Figure 1, an overlay between the X-ray image and 3.5 cm radio contours is shown. X-ray emission from hotspots B and C is coincident with those found in the radio images. Neither of these two hotspots were within the *HST* WFPC2 field of view. The overlays for hotspot A between the X-ray image with the radio contours and the *HST* isophotes are provided in Figures 3a–3c, while Figure 3d shows the X-ray contours on the *HST* image. In both radio observations, hotspot A is offset $2''$ to $3''$ from the X-ray hotspot, similar to what is seen for the case of the *HST* image (Fosbury et al. 1998). A comparison between the optical and the X-ray image reveals an alignment for hotspot A; however, some filaments visible in the *HST* image are not seen in the X-ray image.

A careful examination of the *HST* image reveals an optical hotspot that is less than $1''$ away. The location is indicated by the orange line in Figure 2.

3. X-RAY ANALYSIS

The X-ray spectrum of hotspot A, the diffuse region, and extension E were analyzed using the *Chandra* Interactive Analysis of Observations (CIAO ver. 3.0.2).[6] For hotspots B and C, less than 40 counts were obtained, which is insufficient data to

distinguish between thermal and nonthermal emission processes. The source and background regions were selected, and the spectra of these regions were extracted using the *acisspec* script and imported into Sherpa for modeling. Hotspot A's extracted region is indicated in Figure 4b by the green circular outline with a radius of $3''.5$. The diffuse emission's extracted region is identified by the green annulus with an inner and outer radius of $2''.2$ and $7''.6$, respectively. The cyan rectangular outline with an area of $4''.5 \times 3''.4$ represents the extracted region of extension E.

To obtain an appropriate background that avoids the diffuse region and the hotspots, four circular ($10''$ in radius) regions that are approximately positioned $39''$ to $44''$ northwest, west, south, and northeast from the core were selected. The count rates per square arcsecond are 3.2×10^{-5} counts s^{-1} arcsec^{-2} for the background regions, 2.4×10^{-4} counts s^{-1} arcsec^{-2} for the diffuse region, 5.2×10^{-4} counts s^{-1} arcsec^{-2} for hotspot A, and 6.5×10^{-4} counts s^{-1} arcsec^{-2} for extension E. Uncertainties reported later in this paper for the models' parameters are 1 σ, determined from the Sherpa task *projection*.

3.1. Hotspot A

Shown in Figure 4a is hotspot A's spectrum between 0.30 and 1.35 keV without redshift correction but background subtracted. Initially, a nonthermal model (power law with Galactic absorption) was tested, and the overall residuals indicated a poor fit. Plotted on the spectrum in blue is this nonthermal model. The residuals are shown in the middle panel. The parameters for this power-law model are $\Gamma = 2.6 \pm 0.4$, with a normalization of $(1.1 \pm 0.3) \times 10^{-5}$ and a Galactic neutral hydrogen column density[7] of 2.52×10^{20} cm^{-2}. The reduced χ^2 per degrees of freedom is $\chi^2_{69} = 0.42$.

Further analysis reveals that the Raymond-Smith model for a thermally ionized plasma is appropriate between 0.3 and 1.0 keV. The temperature for this model is $0.22^{+0.04}_{-0.03}$ keV (2.6×10^6 K) with a metal abundance of $[Z/Z_\odot] = 0.10^{+8.24}_{-0.15}$ and $\chi^2_{68} = 0.36$. However, this model was not able to explain a peak between 1.1 and 1.3 keV, so an additional Gaussian component was added to model an emission line. Using the Sherpa package GUIDE for line identification, this emission was identified as Fe xxv, although the uncertainties in the peak are large enough for other possible emission lines (e.g., Fe^{19+}, Ni^{19+}). The error in the model, shown below the spectrum, fluctuates randomly between ± 1.5 σ with a $\chi^2_{65} = 0.33$.

The emission from hotspot A is thermal, based on the comparison between the residuals. Using the *F*-test for a thermal model that excludes and includes the emission line, the significance is ~ 0.05, indicating that the better model involves the emission line. Therefore, the best fit for the hotspot is $(rs + gauss) \times abs$, where *rs* is the XSPEC Raymond-Smith model (*xsraymond*), *gauss* is a simple one-dimensional normalized Gaussian model (*ngauss1d*), and *abs* represents Galactic absorption (*xswabs*). In Figure 4a, the red line plotted on the spectrum is the best model with the residuals in the lowest panel.

3.2. Diffuse Region

The spectrum for the extended region is shown in Figure 4c between 0.3 and 2.6 keV. Once again, a power-law fit was first attempted. This fit was reasonable for the tail of the spectrum between 1.2 and 2.6 keV but poor elsewhere, since the peak in the fit is off from the source spectrum, and the residuals have a
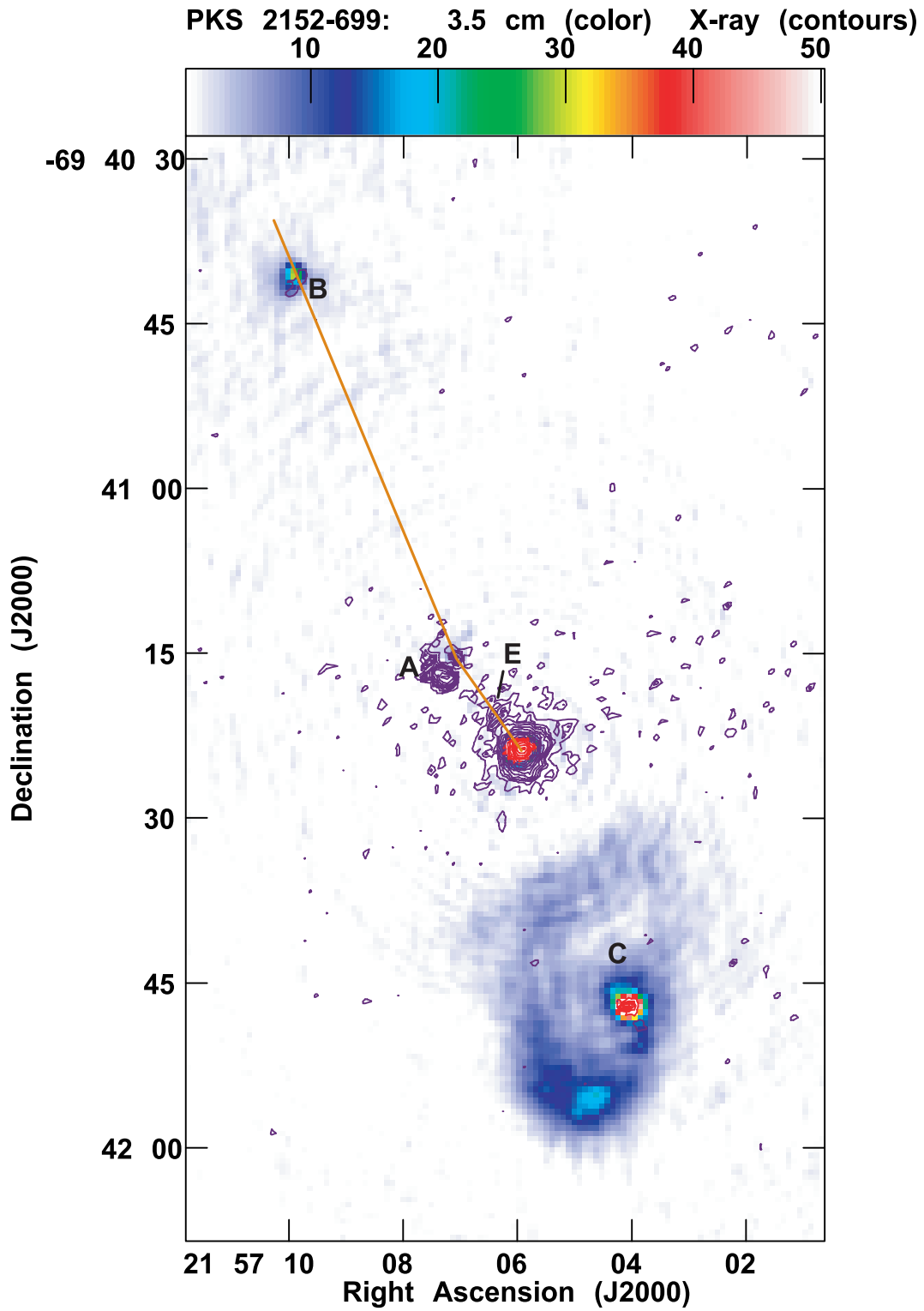
Fig. 1.—Radio (3.5 cm) observation overlayed with X-ray contours of PKS 2152−699. The red and purple contours correspond to regions where the radio flux density is greater than or less than 70% of the peak, 50 mJy beam^{-1}, respectively. Here, three hotspots are detected in both images, with an X-ray−radio coincidence for hotspots B and C. The low-level contours reveal that the diffuse emission is extended more toward hotspot A, and that it is also extended in the west-east direction. The color scale levels range from 0.5 to 50 mJy beam^{-1} with contours levels of 1, 2, 2.8, 4, and 5.7 counts and multiples of $\sqrt{2}$ thereafter. The orange line represents the deflection of the northern jet at hotspot A.
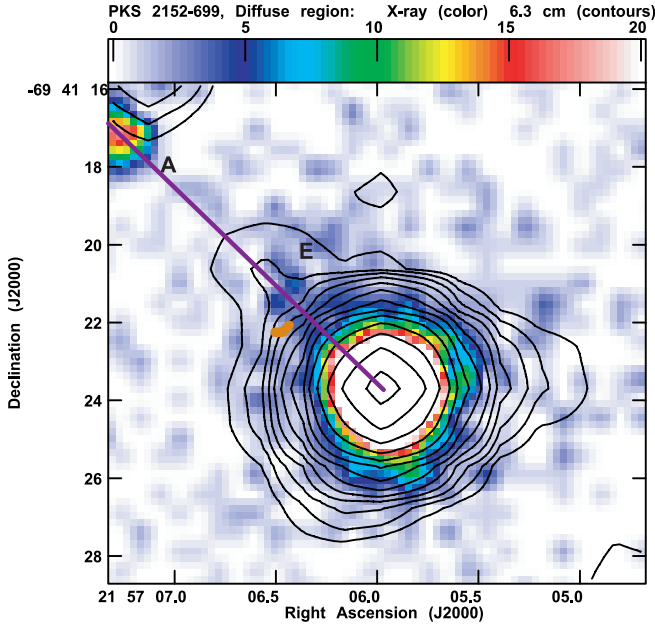
FIG. 2.—Overlay between the X-ray image with 6.3 cm radio contours for the diffuse region. The contour levels are 5 mJy beam^{-1} ×(2, 2.8, 4, 5.7, 8, and multiples of $\sqrt{2}$ thereafter) with the color scale ranging between 0 and 20 counts. The asymmetry in the diffuse emission (labeled as E) is coincident with the radio jet. The purple line represents the radio jet axis, which is also parallel to the X-ray jet and passes through hotspot A's X-ray emission in the upper left. The orange line corresponds to the location of the optical hotspot, with its size indicated by the extent of the line.

"bump" profile between 0.5 and 1.2 keV. The parameters for this nonthermal model are $\Gamma = 1.7 \pm 0.2$ with a normalization of $(3.8 \pm 0.3) \times 10^{-5}$ and $\chi^2_{162} = 0.33$.

Our second attempt was to consider a thermal bremsstrahlung model (*xsbremss*). The profile for this model was similar to the power-law case and hence also a poor fit. This model yielded a goodness of fit of $\chi^2_{162} = 0.30$. The temperature obtained from this fit is $1.4^{+0.5}_{-0.3}$ keV (1.6×10^7 K) with $C = 7.4^{+1.1}_{-1.0} \times 10^{-5}$. Here $C = (3.02 \times 10^{-15}/4\pi D^2) \int n_e n_H \, dV$, where D is the distance to the source in cm, n_e is the electron density in cm^{-3}, and n_H is the hydrogen density in cm^{-3}.

To improve the spectral modeling, the Raymond-Smith model was considered. This fit modeled the data better than the two previous attempts for energies between 0.8 and 1.2 keV, had the lowest χ^2_{154}, 0.28, and the residuals appear flatter. The temperature is $1.04^{+0.28}_{-0.15}$ keV (1.2×10^7 K), with a metal abundance of $[Z/Z_\odot] = 0.07^{+0.06}_{-0.07}$ and a normalization C of $(2.1 \pm 0.4) \times 10^{-4}$. Although all three models look similar in the top plot of Figure 4c, the residuals of the thermal model indicate that the emission is thermal. Hence, $rs \times abs$ is the best model for the diffuse region.

The Raymond-Smith variable model (*xsvraymond*) was considered, and the temperature was similar to the latter attempt. However, it yielded certain metal abundances that were significantly greater than solar abundances with large uncertainties. Although 450 counts were obtained, additional data are needed to better constrain individual metallicities.

Table 1 summarizes the best model for hotspot A and the diffuse region with the nonthermal attempts. The only parameters held fixed during modeling are the known redshift (in the case of *rs*) and the galactic neutral hydrogen density. For the Gaussian model, only an upper limit on the FWHM exists, and it is greater than the expected value.

3.3. *Extension E and PSF Modeling*

Extraction of the northeast extended emission within the diffuse region reveals similar thermal properties as the entire diffuse region. Extension E has an ionized plasma temperature of $1.0^{+3.8}_{-0.5}$ keV (1.1×10^7 K) with an abundance $[Z/Z_\odot]$ of $0.09^{+0.70}_{-0.09}$.

Prior to extracting the PSF, the afterglow[8] events were examined, and were not removed in the final level 2 processing because most of these events were from the core (an additional 170 counts). PSF modeling (using *mkpsf*) of the core at 1.5 keV indicates that the diffuse emission is real compared with the wings of the core. The wings of the normalized PSF fell below one count beyond 2″ from the core, which is within the inner radius of the annulus in Figure 4b.

3.4. *Number Densities and Cooling Times*

3.4.1. *Hotspot A*

The Raymond-Smith model for hotspot A gives a total luminosity of 5.2×10^{40} ergs s^{-1}, or 4.6×10^{40} ergs s^{-1} excluding the Gaussian model. Assuming that the thermal X-ray emission of hotspot A is produced via shock-induced processes (see § 4.1.2), the postshock temperature derived from the Rankine-Hugoniot conditions is

$$T = \frac{3\mu m_p v_{\rm sh}^2}{16k} \Rightarrow v_{\rm sh} = \left(\frac{16kT}{3\mu m_p}\right)^{1/2}, \qquad (1)$$

where $v_{\rm sh}$ is the shock velocity (Landau & Lifshitz 1959). For a temperature of 2.6×10^6 K, the shock velocity is ~480 km s^{-1}. The kinetic energy flux from a shock is $\frac{1}{2}\mu n m_p v_{\rm sh}^3 A_{\rm sh}$, where $A_{\rm sh}$ is the area of the shock region. Assuming that the X-ray luminosity is half the kinetic energy flux and that the shock region consists of the bright area in the X-ray image (Fig. 3) of ~1.3 kpc^2, then the number density is 0.17 cm^{-3}.

The hotspot's emission is projected over a rectangular region outlined in white in Figure 4b. For a projected emitting region of $4\rlap{.}''4 \times 4\rlap{.}''7$ (2.5 kpc × 2.6 kpc) and assuming a depth of 2 kpc, the emitting volume is 13.0 kpc^3 and the power radiated per volume (L_B) by the ionized plasma (excluding the emission line) is 1.2×10^{-25} ergs s^{-1} cm^{-3}. The cooling time for the plasma can be determined from the ratio of the power radiated per volume and the energy density:

$$t_c = \left(\frac{L_B}{E}\right)^{-1} = \frac{n_e kT}{L_B}. \qquad (2)$$

For the numbers reported above, the cooling time for the plasma is approximately 1.6×10^7 yr.

3.4.2. *Diffuse Region*

With the plasma temperature and luminosity known for the region, the electron number density n_e and the cooling time t_c for the diffuse region can be determined. The power radiated per unit volume L_B for a hot plasma is defined as

$$L_B = \frac{L}{V} = \Lambda(T)n_e^2, \qquad (3)$$

---

[8] See the "Remove the acis_detect_afterglow Corrections" thread at http://cxc.harvard.edu/ciao/threads/acisdetectafterglow for more information.
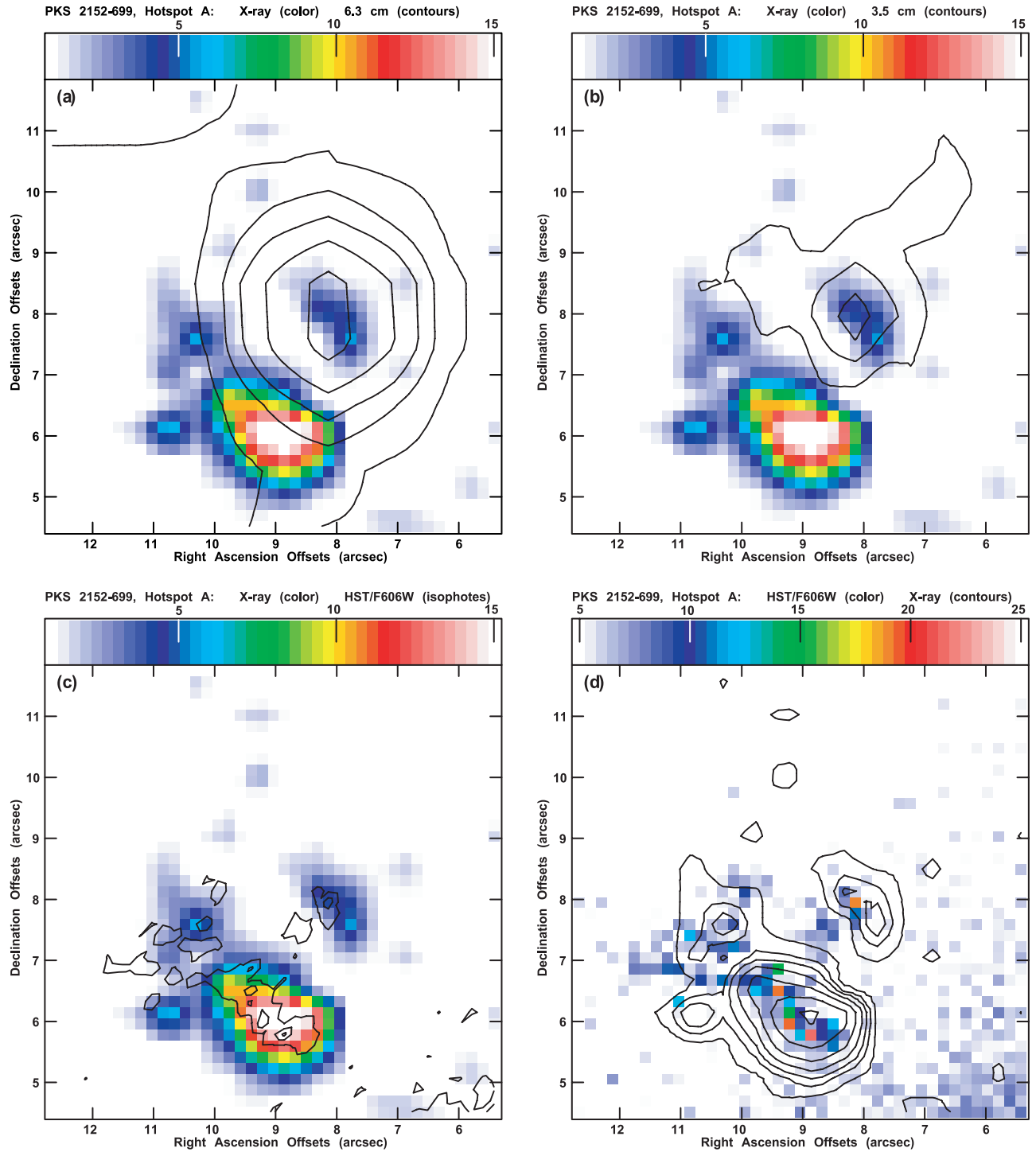
Fig. 3.—Multiwavelength images of hotspot A in PKS 2152−699. The contour levels are scaled from the lowest level by 1, 2, 2.8, 4, 5.7, 8, and multiples of $\sqrt{2}$ thereafter. (*a*) An overlay between the 6.3 cm contours and the X-ray image: the lowest level is 5 mJy beam^{-1}; the color scale levels range from 0 to 15 counts. (*b*) An overlay between the 3.5 cm contours and the X-ray image: the lowest level is 2 mJy beam^{-1}; the color scale levels range from 0 to 15 counts. (*c*) An overlay between the *HST* F606W isophotes and the X-ray image: the lowest level is 7 counts; the color scale levels range from 0 to 15 counts. (*d*) An overlay between the X-ray contours and the *HST* image: the lowest level is 1.5 counts; the color scale levels range from 5 to 25 counts. In (*a*) and (*b*), the radio hotspot is 2″ to 3″ offset from the X-ray hotspot. Here (*c*) and (*d*) reveal an alignment between the optical and X-ray emission for hotspot A with some optical filaments not seen in the X-ray image.
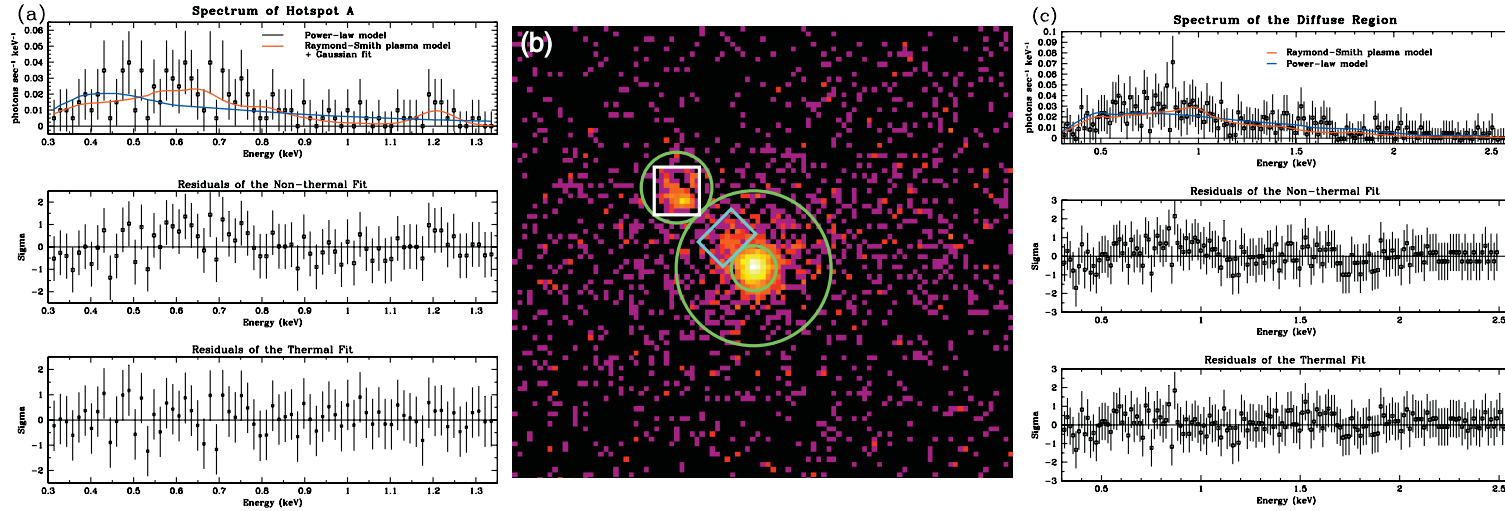
Fig. 4.—X-ray spectra of hotspot A and the diffuse region. (*a*) Hotspot A's spectrum obtained between 0.30 and 1.35 keV. The blue line represents the power-law fit, and the red line represents the best fit, a Raymond-Smith model with a Gaussian centered at 1.2 keV. This emission line may correspond to Fe xxv. Below the spectrum are the σ residuals of the fits between 0.30 and 1.35 keV. The extracted regions, outlined in green, are shown in (*b*), and the emitting volume for hotspot A projected on the sky is shown by the white box. The cyan box indicates the region where extension E's spectrum was obtained to compare with the diffuse region. It is also the projected emitting region. (*c*) Diffuse region's spectrum between 0.3 and 2.6 keV with the residuals of the fits below it. The red and blue lines correspond to the Raymond-Smith and the power-law models, respectively.

TABLE 1
PARAMETERS FOR THE SHERPA MODELS

Parameter (1)	Value (2)	Lower Bound (3)	Upper Bound (4)
Hotspot A			
$(rs + gauss) \times abs$	$\chi^2_{65} = 0.33$	...	...
Raymond-Smith Model (rs):			
T (keV)	0.22	0.03	0.04
$[Z/Z_\odot]$	0.10	0.15	8.24
C	1.1×10^{-4}	1.0×10^{-4}	0.9×10^{-4}
Gaussian Model (gauss):			
E_0 (keV)	1.20	0.05	0.04
FWHM	0.005	...	0.31
A	1.6×10^{-6}	1.0×10^{-6}	1.1×10^{-6}
$plaw \times abs$	$\chi^2_{69} = 0.42$	...	...
Power-law Model (plaw):			
Γ	2.6	0.4	0.4
B	1.1×10^{-5}	0.3×10^{-5}	0.3×10^{-5}
Diffuse Region			
$rs \times abs$	$\chi^2_{154} = 0.28$	...	...
Raymond-Smith Model (rs):			
T (keV)	1.04	0.15	0.28
$[Z/Z_\odot]$	0.07	0.07	0.06
C	2.1×10^{-4}	0.4×10^{-4}	0.4×10^{-4}
$plaw \times abs$	$\chi^2_{162} = 0.33$	...	...
Power-law Model (plaw):			
Γ	1.7	0.2	0.2
B	3.8×10^{-5}	0.3×10^{-5}	0.3×10^{-5}

NOTES.—Parameters used in the Sherpa models for hotspot A and the diffuse region. Col. (1) contains the parameters for the model, Col. (2) indicates the corresponding values, and Cols. (3) and (4) report the lower and upper 1 σ uncertainties. Here rs is the Raymond-Smith model, $plaw$ is a power-law model, and $gauss$ is the one-dimensional Gaussian model. In col. (1), T is the plasma temperature, Z is the metallicity with respect to solar abundances, $C = (3.02 \times 10^{-15}/4\pi D^2) \int n_e n_H \, dV$, E_0 is the center of the Gaussian peak, FWHM is the full-width at half maximum of the Gaussian peak, A is the amplitude of the Gaussian normalization, and B is the amplitude of the power-law model. The χ^2_ν for each modeling attempt is reported.

where $\Lambda(T)$ is the total cooling coefficient in units of ergs cm^3 s^{-1} and V is the volume of the emitting region. For a temperature of $\sim 10^7$ K, Λ is approximately 7×10^{-23} ergs cm^3 s^{-1} (Raymond et al. 1976).

For the diffuse emission without the extension, assuming that the volume is spherically symmetric and that the emitting region is projected onto the sky as an annulus, the volume is 305 kpc^3. The luminosity of the diffuse emission is 1.4×10^{41} ergs s^{-1}. This implies a number density of 0.01 cm^{-3} and a cooling time of 5.1×10^7 yr.

The greatest uncertainty in our calculations is in the size of the emitting region. The emitting region used in our calculation is (6.7 kpc)^3. The proportionality between n_e and t_c with the volume is

$$n_e \propto V^{-1/2}, \text{ and} \tag{4}$$

$$t_c \propto V^{1/2}. \tag{5}$$

Thus, a factor of 2 in the volume will only decrease n_e and increase t_c by a factor of $\sqrt{2}$.

For the extended section of the diffuse emission (indicated by the cyan box), the emitting volume is 9.8 kpc^3 when assuming that the depth is 2 kpc, and the luminosity is 3.2×10^{40} ergs s^{-1}.

The number density for the extended region in the diffuse emission is then 0.04 cm^{-3} with a cooling time of 1.8×10^7 yr.

3.4.3. Broadband Flux Plot

Figure 5 reveals the broadband flux (between radio and X-ray) for the northwestern component of hotspot A as seen in Figure 3. Radio, optical, and X-ray emission overlap at this position. An additional measurement at 5472 Å was reported by di Serego Alighieri et al. (1988). The upper limit infrared (IR) fluxes from *IRAS* observations were provided by Golombek et al. (1988) at 12 and 100 μm. PKS 2152−699 was detected at 25 and 60 μm, but these are not included in Figure 5 because the poor resolution of *IRAS* could not distinguish possible IR emission of hotspot A from the core. The optical flux of the *HST* F606W observation is primarily [O III], [N II], and Hα emission lines (Fosbury et al. 1998).

4. INTERPRETATION

4.1. Hotspot A

The thermally ionized volume of gas is located ∼5.6 kpc from the nucleus of the parent galaxy (Fosbury et al. 1998), and there are two possible explanations that can account for the presence of X-ray emission at this distance. One explanation considers the possibility that hot material from the inner regions of the interstellar medium (ISM) is advected out to this location by the radio jet and the other is the jet-cloud interaction mentioned above.

4.1.1. Entrainment from Inner Regions

The gas could have been entrained and heated from the dense ISM in the inner regions of the galaxy by the outflowing jet. This process is virtually unavoidable over a wide variety of physical parameters (e.g., De Young 2002). If entrainment is to explain the X-ray emission from hotspot A, then the cooling time of the gas must be approximately equal to the transit time of the entrained material so that the X-ray emission is visible only at the end of the entraining region.

However, the fact that no corresponding thermal X-ray emission is seen to the south requires special arrangements to exist, presumably in the form of different conditions in the inner ISM for the north jet than for its southern counterpart. In addition, in this picture the proximity of radio and X-ray emission at hotspot A must be regarded as a fortuitous coincidence. These issues, together with the interpretation of the diffuse X-ray emission near the nucleus in the direction of the radio jet (see § 4.2), lead us to believe that the most plausible interpretation of the X-ray and radio morphology at hotspot A is that of a jet-cloud interaction.

4.1.2. Jet-Cloud Interaction

The thermal emission could arise from the interaction of the radio jet and a relatively dense cloud of ambient gas located in the path of the oncoming jet. This latter possibility was suggested by Fosbury et al. (1998) as a mechanism to explain both the optical emission lines in the inner cloud and the apparent misalignment between the inner and outer northern radio hotspots. The mass of the cloud is $5.3 \times 10^7 \, M_\odot$, which is reasonable for large clouds in the ISM (Young & Scoville 1991). The mass could be even larger and still be within conventional limits for giant clouds. The collapse time for this cloud due to its own self-gravity is 1.6×10^8 yr, an order of magnitude longer than the cooling time but much shorter than the age of the parent galaxy.
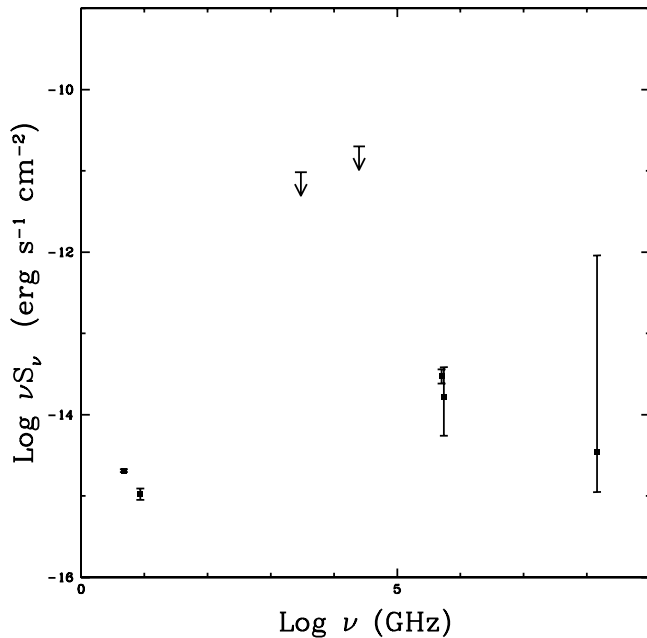
Fig. 5.—log-log plot of the broadband flux νS_ν (ergs s^{-1} cm^{-2}) as a function of frequency ν (GHz) for the unresolved northwestern component of hotspot A. The upper limits were provided by Golombek et al. (1988) at 12 and 100 μm, and di Serego Alighieri et al. (1988) provided a measurement at 5472 Å.

A jet-cloud interaction can also explain both the presence of radio emission colocated with the thermal X-ray emission, as well as account for the misalignment. A grazing encounter between collimated supersonic flow and a dense object will give rise to internal shocks in the flow as it is deflected away from the massive object. These shocks will cause enhancements of both the relativistic particle and magnetic field densities and will result in a significant brightening of the synchrotron radiation of the jet, giving rise to a radio hotspot.

The interaction will also cause a shock to propagate into the cloud as it deflects the jet. This shock-heated gas will cool rapidly in the high-density cloud, emitting thermal X-rays and highly ionized emission lines as seen in this *Chandra* observation. This hot, postshock gas will reside in the cloud and be adjacent to, but not exactly coincident with, the jet. Thus, the offset between the radio and X-ray emission is naturally explained by this mechanism.

Furthermore, the geometry of this offset is also consistent with a 20° jet deflection. The northernmost radio hotspot is offset to the west from a straight line between the nucleus and hotspot A, and its radio emission is also offset to the west from the X-ray emission. This is consistent with the jet grazing the cloud on the west side, deflecting the jet to the west of the original radio-jet axis (see Fig. 1) and causing a shock to propagate into the interior of the cloud, most of which lies east of the contact point (see Fig. 3).

The shallow grazing incidence of the jet on the cloud will produce a weaker shock propagating into the cloud. This interaction is consistent with the temperature derived here for the thermal emission, $T \sim 10^6$ K, since such a postshock temperature implies shock speeds of a few hundred km s^{-1}, which are very much less than the probable jet speed of over 1000 km s^{-1}.

Numerical simulations of the interaction of the radio jets with dense clouds provide support for the latter picture, although the parameters of these calculations may not fit the exact values required for the case of PKS 2152−699. For example,

Wang et al. (2000) consider interactions with very dense clouds, hundreds to thousands of times the jet density, and find that jets tend to be destroyed or disrupted by very massive clouds. Longer term deflections occur if the cloud-jet density ratios are less extreme and the Mach numbers are not large (De Young 1991; Higgins et al. 1999), although in some cases the cloud can be destroyed by the jet if the cloud is sufficiently underdense or of small mass. Clouds of $\sim 10^7 M_\odot$ with densities on the order of 100 times the jet density can survive over 10^7 yr when deflecting jets with speeds in excess of 10^3 km s^{-1}. Therefore, long-term jet deflection, especially for the small apparent deflection angles seen here, can probably be produced from a combinations of reasonable jet speeds, jet-cloud density ratios, and total cloud masses.

Although both the entrainment and deflection pictures are physically plausible, the north-south asymmetry of the radio jets and the presence of thermal X-ray emission suggest that the simplest interpretation may well be that the northern jet of PKS 2152−699 is slightly deflected by a massive interstellar cloud, and this deflection is producing shock-heated gas in the cloud, which manifests itself via the thermal X-ray emission reported in this paper.

4.2. *Diffuse Emission*

As discussed in the observational section, there is a faint X-ray extension of the diffuse emission in the direction of the radio jet. This emission appears to be thermal rather than nonthermal, and the temperature and metal abundance for this extension is the same as that of the rest of the diffuse emission. The number density in this extension is roughly 0.04 cm^{-3}, which is 4 times greater than the diffuse emission as a whole. It appears that this X-ray–emitting material in the extension could well be the same hot gas as that around the galaxy that is giving rise to the overall diffuse X-ray emission.

A nearby optical hotspot is seen, and it may be that the extension is due to the same process as in hotspot A of a jet interacting with a dense cloud. However, since extended thermal emission (representable as hot gas) is present next to the core, it is likely that the gas may also be extrained by the jet, tracing out an extension.

To summarize, the radio morphology of the northern jet and the radio–X-ray misalignment for hotspot A would indicate a jet-cloud interaction. Moreover, thermal emission for hotspot A is explained by shocks formed in the clouds when this interaction occurs. This interaction may also be occurring at extension E, where the optical image reveals an EELR.

5. FUTURE OBSERVATIONS

This 14 ks observation of PKS 2152−699 detected three hotspots and diffuse emission around the core. Although this observation was sufficient to confirm thermal emission from hotspot A, a longer observation is needed to constrain its metallicity and to determine the ambiguous emission line at approximately 10 Å. Moreover, additional time will help distinguish whether thermal or nonthermal emission is detected in the two farthest hotspots, and it will help understand the content of the inner ISM from improved modeling of the diffuse region. Additional *HST* observations of hotspots B and C are needed, since the optical flux will constrain the mechanisms for the detected X-ray emission.

Other sources that are believed to have undergone jet-cloud interactions should be investigated for their X-ray emission properties. For example, radio and optical observations of

Coma A (3C 277.3) have indicated a jet-cloud interaction from the coincidence of the emission-line gas and its double-radio lobes (van Breugel et al. 1985). There is also strong support for jet-cloud interactions for high-redshift ($z > 0.6$) radio galaxies (Tadhunter 2002 and references therein). However, these sources have larger redshifts compared to PKS 2152−699, hence thermal emission may not be detected because these sources are more distant, and the inverse-Comptonization of the CMB photons is more prominent.

6. CONCLUSION

From previous X-ray observations of extended emission from extragalactic radio sources, only nonthermal processes, such as inverse-Compton, synchrotron self-Compton, and synchrotron radiation, are believed to be the cause of X-ray (and possibly optical) emission from kiloparsec or megaparsec hotspots and jets (Harris & Krawczynski 2002; Wilson 2003). However, the X-ray observation of PKS 2152−699 contradicts accepted ideas about X-ray emission mechanisms. This observation reveals that thermal processes are dominant for hotspot A and a diffuse region around the core with an extension (much like a jet). Spectral modeling of the hotspot reveals a Raymond-Smith plasma of 2.6×10^6 K with an additional iron (or possibly nickel) emission line. The diffuse region can also be modeled as a hot plasma of 1.2×10^7 K.

To explain the detection of thermal emission for hotspot A, it is believed that a jet-cloud interaction is occurring at the site of hotspot A. The deflection of the northern jet and hotspot and the offset between radio and X-ray emission for hotspot A are evidence to support such an interaction. Moreover, as the jet collides with the cloud, shocks are likely to propagate into the cloud, thus heating it. As the cloud cools rapidly, thermal X-rays, as reported in this paper, are emitted.

A comparison between the radio and X-ray images for the diffuse region reveals that it is extended in the northeast direction, with similar thermal properties as the diffuse emission. With a detected EELR near extension E, one possible explanation is that the jet is interacting with the cloud. However, there is a possibility that hot gas (as seen by the diffuse emission) from the inner ISM is entrained by the jet, and this will contribute to the X-ray emission.

This is the first detection of extended thermal emission on extragalactic scales from a diffuse region and hotspot. Other radio sources believed to have undergone jet-cloud interaction should be investigated for possible thermal X-ray emission.

REFERENCES

Bennett, C. L., et al. 2003, ApJS, 148, 1
Biretta, J. A., et al. 1996, WFPC2 Instrument Handbook, Version 4.0 (Baltimore: STScI)
De Young, D. S. 1991, ApJ, 371, 69
———. 2002, The Physics of Extragalactic Radio Sources, (Chicago: Univ. Chicago Press)
di Serego Alighieri, S., Binette, L., Courvoisier, T. J.-L., Fosbury, R. A. E., & Tadhunter, C. N. 1988, Nature, 334, 591
Fanaroff, B. L., & Riley, J. M. 1974, MNRAS, 167, 31P
Fosbury, R. A. E., Morganti, R., Wilson, W., Ekers, R. D., di Serego Alighieri, S., & Tadhunter, C. N. 1998, MNRAS, 296, 701
Golombek, D., Miley, G. K., & Neugebauer, G. 1988, AJ, 95, 26
Harris, D. E., & Krawczynski, H. 2002, ApJ, 565, 244
Higgins, S. W., O'Brien, T. J., & Dunlop, J. S. 1999, MNRAS, 309, 273
IERS. 1999, 1998 Annual Report, ed. D. Gambis (Paris: Obs. Paris), 87
Landau, L. D., & Lifshitz, E. M. 1959, Fluid Mechanics (London: Pergamon)
Ma, C., et al. 1998, AJ, 116, 516

Raymond, J. C., Cox, D. P., & Smith, B. W. 1976, ApJ, 204, 290
Solórzano-Iñarrea, C., & Tadhunter, C. N. 2003, MNRAS, 340, 705
Tadhunter, C. N. 2002, Rev. Mexicana Astron. Astrofis. Ser. Con., 13, 213
Tadhunter, C. N., Fosbury, R. A. E., di Serego Alighieri, S., Bland, J., Danziger, I. J., Goss, W. M., McAdam, W. B., & Snijders, M. A. J. 1988, MNRAS, 235, 403
Tadhunter, C. N., Villar-Martin, M., Morganti, R., Bland-Hawthorn, J., & Axon, D. 2000, MNRAS, 314, 849
Tingay, S. J., et al. 1996, AJ, 111, 718
van Breugel, W., Miley, G., Heckman, T., Butcher, H., & Bridle, A. 1985, ApJ, 290, 496
Villar-Martín, M., Tadhunter, C., Morganti, R., Axon, D., & Koekemoer, A. 1999, MNRAS, 307, 24
Wall, J. V. 1994, Australian J. Phys., 47, 625
Wang, Z., Wiita, P. J., & Hooda, J. S. 2000, ApJ, 534, 201
Wilson, A. S. 2003, NewA Rev., 47, 417
Young, J. S., & Scoville, N. Z. 1991, ARA&A, 29, 581